Early plume expansion in atmospheric pressure midinfrared laser ablation of water-rich targets

Zhaoyang Chen and Akos Vertes*
Department of Chemistry, The George Washington University, 725 21-st Street, N.W., Washington, DC 20052, USA
(Received 16 October 2007; published 25 March 2008)

We have developed a one-dimensional fluid dynamics model for the ablation of water-rich targets by nanosecond infrared laser pulses at atmospheric pressure. To describe the laser-target interaction and the plume expansion dynamics, in light of recent experimental results the model incorporates phase explosion due to superheating and the nonlinear light absorption properties of water. In the model, the phase explosion is treated as a prolonged process that lasts for a finite time. Once a thin layer beneath the target surface exceeds the phase explosion temperature, this layer is transformed from target material into a mixture of water vapor and droplets and become part of the plume. This process is sustained for some time until the laser energy cannot maintain it. The simulation results show that as a result of two different phase transition mechanisms, i.e., surface evaporation and phase explosion, a first, slower plume expansion phase is followed by a more vigorous accelerated expansion phase. The calculated time evolution of the shock front at various fluence levels agrees well with the experimental observations of Apitz and Vogel [I. Apitz and A. Vogel, Appl. Phys. A. **81**, 329 (2005)]. This model sheds light on the effect of phase explosion in laser ablation dynamics and its results are relevant for material synthesis, surface analysis, and medical (surgery) applications.

DOI: 10.1103/PhysRevE.77.036316 PACS number(s): 47.60.−i, 64.70.F−, 52.38.Mf, 79.20.Ds

I. INTRODUCTION

Experimental and theoretical investigations of laser ablation (LA) in the presence of a background gas are aimed at trying to understand the regimes and processes in this strongly nonlinear interaction (e.g., thermal vs electronic vs mechanical effects, particle formation, surface evaporation vs phase explosion, plasma ignition, etc.) [1–14]. Meanwhile, LA is used for a growing number of applications, such as pulsed laser deposition (PLD) for thin film growth [8], cluster production, matrix-assisted pulsed laser evaporation (MAPLE) for the growth of organic films [15], micromachining [16], laser surgery [17], nanoparticle synthesis [18], and chemical analysis [19,20]. Specifically, midinfrared laser ablation of water-rich targets is utilized for preparative (MAPLE) [21], medical [22], and analytical applications [19,23]. For example, atmospheric pressure matrix-assisted laser desorption ionization (AP-MALDI) is being explored as an efficient way to produce ions and neutrals for mass analysis [23–26]. The understanding of LA dynamics and plume expansion in the presence of an ambient gas is a key issue for these applications. However, the interaction of the plume with the ambient gas compared to expansion into vacuum is a far more complex gas-dynamic process [27].

Surface evaporation is considered to be a major mechanism for material removal during the LA process. However, if the laser energy deposition into the target is fast enough (e.g., in case of nanosecond or shorter laser pulses), the target can be temporarily superheated to a temperature far beyond its thermodynamic boiling point. When the temperature of a layer reaches the phase explosion temperature [28], then it may be directly transformed from liquid water into a mixture of vapor and liquid droplets. Due to its increased volume, this layer is ejected from the target. This material removal mechanism, called phase explosion [2,28–30], is radically different from surface evaporation.

The absorption of laser light by water below the surface plays an important role during water ablation and phase explosion. The absorption of mid-IR laser radiation in the fluence range of interest for water ablation is nonlinear (see Ref. [31] and the references therein). Shori *et al.* [31] found that the dynamic changes in the absorption coefficient of liquid water are a function of the incident fluence. Specifically, the absorption coefficient decreases with increasing fluence. Whereas the linear (low fluence) absorption coefficient of liquid water at 2.94 μm wavelength is 1.33×10^4 cm^{-1} at fluence of 1.0 J/cm^2, the effective absorption coefficient is only 0.8×10^4 cm^{-1}. At 0.8 J/cm^2 laser fluence, the transmission of a 4.26 μm thick water layer increases from the low fluence value of ~0.5% to 11%. Presumably, at these higher fluences the hydrogen bond network of water is disrupted by heating and this is reflected in a blue shift of the absorption resonance. Although considered profound, the effect of nonlinear light absorption on the ablation dynamics is typically neglected by fluid dynamics models. In the presented model, the nonlinear light absorption properties of water are also incorporated.

Recently, fast imaging results on laser ablation of water, liver, and skin utilizing a Q-switched Er:yttrium-aluminum-garnet (YAG) laser were reported by Apitz and Vogel [22]. Their experimental observations confirm that the whole ablation process proceeds through three partially overlapping stages. Initially, nonequilibrium surface evaporation occurs. Later when the laser irradiance is increased to a certain value, the target experiences a fast heating process and phase explosion of the superheated subsurface layer starts. The formed plume in this stage is moving faster than in the first stage. At times later than 1 μs further material expulsion occurs due to the recoil pressure induced by the phase explosion and by other fluid instabilities. In this paper, we will focus our attention mainly on the first and second stages of the ablation.

*Corresponding author.

Although there have been some theoretical and numerical studies on the phase explosion phenomenon in general, these studies do not address midinfrared laser ablation. Moreover, the incorporation of phase explosion into fluid dynamics is still a largely unexplored area. A one-dimensional (1D) fluid model for the nanosecond laser ablation of metals in 1 atm nonreactive ambient gas was previously developed to consider the ionization of both the ablated material and the ambient gas during the early stage of plume expansion [32]. More recently, we have extended this model for the description of phase explosion during water ablation by an IR laser pulse [33]. However, in this earlier study the phase explosion that in reality may last for a finite time, was treated as an instantaneous event. In this paper, we refine this model by considering a prolonged phase explosion process in the mid-IR laser ablation of water-rich targets at atmospheric pressure. During this prolonged phase explosion process, multiple layers of water experience phase explosion one by one until the decaying laser irradiance cannot sustain such a process. The resulting fluid dynamics model, believed to be also applicable in ultrafast laser ablation [20], provides insight into the effect of phase explosion on plume expansion dynamics. In this paper, we apply this model to mid-IR laser ablation of water at various laser fluences and compare the simulation results with experimental data. Through such comparisons, different energy dissipation mechanisms and their influence on plume expansion are clarified.

II. MODELING METHODS

A. Condensed phase processes

As a first step, a 1D fluid dynamics model was applied to water ablation into 1-atm nitrogen background gas. The 1D approach simplifies the equations of fluid dynamics and reduces computation time by neglecting the plume expansion in the radial direction. This approximation is most appropriate at early times and close to the expansion axis but it limits the applicability of our model to the first microsecond. The expanding plume in case of a point source appears spherical and the radial transport of energy and material is very important. Our calculations, however, are concerned with modeling experiments where the focal spot size of the laser beam is between 0.5 and 1.0 mm. Thus, at short times and close to the beam axis the expansion is quasi one dimensional (i.e., it is more disklike than spherical). Even at the end of the period of our calculations, i.e., at 1000 ns, the axial plume dimensions ($\sim$0.4 mm, $\sim$1.2 mm, and $\sim$1.4 mm for 0.12 J/cm^2, 1.4 J/cm^2, and 5.4 J/cm^2, respectively) are still comparable to the laser spot size. At significantly longer times the laser spot can be treated as a point source and the three-dimensional effects become more important.

Furthermore, the laser pulse with 70 ns pulse length at full width at half maximum (FWHM) deposits energy into the target for $\sim$200 ns. Thus, compared to the 1000 ns time domain of the calculations, the energy deposition cannot be considered instantaneous. Due to the fact that the boiling temperature of water is relatively low, the surface evaporation process continues beyond 1000 ns. This evaporation drives the plume in a forward direction and also works against a spherically symmetric expansion.

The laser-target interaction can be described by the heat transport equation with a penetrating source (laser energy directly absorbed by the target below surface). Due to the evaporation process, the target surface recedes into the target. The 1D heat transport equation in a reference frame, which moves at a velocity $u(t)$ and is attached to the liquid-vapor interface is

$$c_p\rho\left[\frac{\partial T(t,x)}{\partial t} - u(t)\frac{\partial T(t,x)}{\partial x}\right] = \frac{\partial}{\partial x}\lambda\frac{\partial T(t,x)}{\partial x} + (1-R)\alpha I(t)\exp(-\alpha|x|). \quad (1)$$

The notations used in Eq. (1) are as follows: x—coordinate along the normal to the target surface, C_p—specific heat capacity, λ—heat conductivity, R—surface reflectivity, ρ—mass density, T—temperature, $I(t)$—laser irradiance at the target surface, and α—optical absorption coefficient of the liquid. The effect of the dynamic changes in the condensed phase optical absorption coefficient, α, in Eq. (1) is not trivial, since the effective absorption coefficient changes up to an order of magnitude as a function of energy density deposited at different depths [31]. In this paper, the nonlinear α is applied to calculate the temperature distribution in the target in the following way: (1) a linear absorption coefficient is initially set up for all depths; (2) the nonlinear absorption coefficient at different depths at the next time step is obtained by evaluating the energy deposited into the corresponding layer in the current time step and this procedure is repeated as time evolves. This nonlinear absorption coefficient, in general, is a function of and decreases with increasing the local temperature. Such behavior of the absorption coefficient results in the formation of a thicker superheated layer.

Furthermore, special attention is paid to the mass density and the specific heat capacity, since they can change greatly with temperature. The temperature dependence of the mass density and the specific heat capacity of water used in the simulations is obtained from the interpolation of tabulated values [34] and is shown in Fig. 1. One can see that the specific heat capacity of water increases dramatically when the temperature is higher than 600 K. The dramatic increase of the specific heat capacity at high temperature reflects that the material is approaching its critical point. For the experimental fluence range of water ablation with Q-switched Er:YAG laser pulses (a few J/cm^2), the rate of energy deposition into the target is high enough to superheat the liquid to the phase explosion temperature. Once this temperature is reached, the phase explosion process occurs and a significant volume of the target abruptly transforms from superheated liquid into a mixture of liquid droplets and vapor. This mixture is then directly ejected from the target.

B. Plume dynamics

The 1D plume expansion dynamics can be described by a set of equations for the conservation of mass, momentum

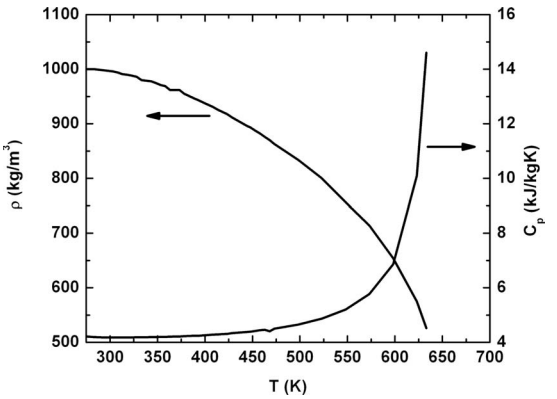

FIG. 1. Mass density and constant pressure specific heat capacity of liquid water as a function temperature.

and energy and vapor transport for a binary mixture, as follows [32,33]:

$$\frac{\partial \rho_t}{\partial t} = -\frac{\partial \rho_t v}{\partial x}, \tag{2}$$

$$\frac{\partial \rho_v}{\partial t} = -\frac{\partial \rho_v v}{\partial x} + \frac{\partial}{\partial x}\left(\rho_t D_{ab} \frac{\partial}{\partial x}\omega_v\right), \tag{3}$$

$$\frac{\partial \rho_t v}{\partial t} = -\frac{\partial}{\partial x}\left(\rho_t v^2 + P + \frac{\partial}{\partial x}\tau_{xx}\right), \tag{4}$$

$$\frac{\partial}{\partial t}\left[\rho_t\left(U + \tfrac{1}{2}v^2\right)\right] = -\frac{\partial}{\partial x}\left[\rho_t\left(U + \tfrac{1}{2}v^2\right)v + Pv\right] - \frac{\partial}{\partial x}(q + v\tau_{xx}) + \alpha_v I(t). \tag{5}$$

Here ρ_t, ρ_v, and ρ_b, which satisfy the relation $\rho_t = \rho_v + \rho_b$, represent the plume mass density, the water vapor density, and the background gas mass density, respectively. v, $\rho_t U$, and P are the local velocity, energy density, and pressure in the plume, respectively. The water vapor mass density fraction is expressed by $\omega_v = \rho_v / \rho_t$, the relevant component of the momentum flux tensor is τ_{xx} and D_{ab} is the binary diffusivity of the mixture. The diffusion caused by pressure is neglected here because it is much smaller than the corresponding term due to the mass density gradient. α_v stands for the highly density-dependent light absorption coefficient in the vapor phase. This coefficient can be approximated based on the product of the condensed phase absorption coefficient in Eq. (1) and the ratio of vapor density to liquid density of water at the same temperature. When the number density of water molecules in the plume is much smaller than that of the liquid, α_v decreases to zero. The energy flux, q, is defined as follows [32]:

$$q = -\lambda \frac{\partial T}{\partial x} - \sum H_i \rho D_{ab} \frac{\partial \omega_i}{\partial x}, \tag{6}$$

where λ is the thermal conductivity of the binary mixture, H_i is the component enthalpy on a mass basis. The thermal conductivity and the binary diffusivity as well as the viscosity of the binary mixture can be calculated based on the component number densities and the local pressure.

The 1D calculation domain consists of two parts: the target and the plume domain, each composed of a few thousand discrete cells. Equation (1) is solved with a second-order central difference method, whereas Eqs. (2)–(5) are solved with the combination of the first-order Godunov method (for the convective terms) and a first-order central difference method (for the diffusion, viscosity, and thermal conduction terms). All the equations are simultaneously solved numerically. During the period of surface evaporation, the boundary conditions for Eqs. (1)–(5) are treated the same as in Ref. [32]. The vaporization flux, F, is governed by the Hertz-Knudsen equation and it is written as follows:

$$F = \frac{f p_0}{\sqrt{2\pi m k T_s}} \exp\left[\frac{H_{ev} m}{k}\left(\frac{1}{T_b} - \frac{1}{T_s}\right)\right], \tag{7}$$

where T_b is the boiling temperature of water at p_0 pressure, H_{ev} is the heat of vaporization, m is the mass of a water molecule, T_s is the water surface temperature, k is the Boltzmann constant, and f is the vaporization coefficient.

The Knudsen layer (KL) theory is applied to connect the surface vaporization condition and the left boundary condition of the first cell in the plume domain. The number density, pressure, and the temperature at the exit of the KL are connected with the surface saturation density, saturation pressure, and surface temperature. Since the condition of the surface varies with time, the values (number density, temperature, and velocity) at the exit of the KL are calculated and used as the property of the influx of the plume domain. The real influx to the plume domain is calculated based on the Hertz-Knudsen equation and the KL theory. After the laser pulse ceases, the target surface temperature drops gradually. When the surface saturation pressure (obtained from the Clausius-Clapeyron equation) drops below the pressure of the plume close to the target surface, recondensation occurs. As it has been proven for polymer ablation, this process can last much longer in time than the ablation process and it reduces the plume density close to the target surface. It can also deposit ablated material outside the area of the laser focal spot [35].

C. Phase explosion

Due to heat loss through evaporation at the surface and as a result of the nonlinear absorption of the laser light in the target, the temperature below the surface can exceed its value at the surface. For nanosecond laser pulses, the energy deposition into the target might be fast enough to superheat a subsurface layer. Once the temperature exceeds the liquid phase explosion temperature, 0.8 to $0.9T_c$ (T_c is the critical temperature, approximately equal to 647 K for water), the corresponding layer experiences a sudden decomposition called phase explosion [9]. The actual phase explosion temperature depends on the pressure. As the actual pressure of the superheated liquid under pulsed laser irradiation is difficult to evaluate [29], in this paper, we use a lower limit for the phase explosion temperature, $0.8T_c$ (517.6 K), in all the calculations. Experience with the model showed no signifi-

cant influence of choosing a particular phase explosion temperature between $0.8T_c$ and $0.9T_c$ on the plume expansion. Note that in Ref. [33] $0.9T_c$ was used as the phase explosion temperature.

When the phase explosion process starts, the computational domains are modified. The liquid-vapor interface at this moment is instantaneously shifted to the location that separates the cells with temperatures above and below $0.8T_c$. From this cell inwards, the temperature decreases gradually from $0.8T_c$ to room temperature and Eq. (1) can be applied to describe the laser target interaction. On the other side of this cell, however, the liquid layer is instantaneously converted into vapor (phase explosion) and it becomes part of the plume calculation domain. The temperatures in these cells are directly used for the plume domain. The number density of water vapor in these cells is obtained from the number density of water in the liquid state. After the phase explosion starts, the process described above is repeated until the phase explosion stops due to the decline of energy deposition by the decaying laser pulse. This approach enables the description of a continuous layer-by-layer phase explosion process. During phase explosion the KL boundary condition is not used across the new interface separating the liquid and the vapor. Once the phase explosion is over, the algorithm returns to solve for the surface evaporation process and plume expansion.

There are two energy dissipation mechanisms in the interaction of mid-IR laser pulse with water: a surface and a volume process. The application of Taylor's similarity theory for spherical explosions to the experimental data allowed us to analyze the energy deposition mechanisms in detail. Taylor's model predicts the time dependence of the shock front position [36] as $R(t)=S(\gamma)\rho_b^{-1/5}E^{1/5}t^{2/5}$, where $S(\gamma)$ is a weak function of the specific heat ratio, γ, of the background gas, ρ_b is the background gas density, and E is the deposited energy. Plotting the experimental $R(t)$ data as a function of $t^{2/5}$ produced two linear sections. From the ratio of their slopes, s, we determined the ratio of energies dissipated in the surface, E_s, and volume, E_v, processes as $s=(1+E_v/E_s)^{1/5}$. The deposited laser pulse energy, $E=E_v+E_s$, drives both of these processes, therefore, knowing the total fluence of the laser pulse and the slope ratio, s, we were able to calculate the two energy fractions. Furthermore, the approximate onset time of the volume process (i.e., the phase explosion) can be extracted by back extrapolating the corresponding segment of the $R(t)$ vs $t^{2/5}$ plot. The actual estimated phase explosion onset times for the studied intermediate, 1.4 J/cm^2, and elevated, 5.4 J/cm^2, laser fluences were 87 ns and 122 ns, respectively. As our model does not predict the onset time of the phase explosion, these values can be used as initial estimates in the fluid dynamics simulations.

III. MODELING RESULTS

A. Intermediate ablation regime

Calculations were carried out for the ablation of water by Q-switched Er:YAG laser pulses ($\lambda=2.94$ μm and $\tau=70$ ns FWHM) at various fluence levels below and above the onset of phase explosion.

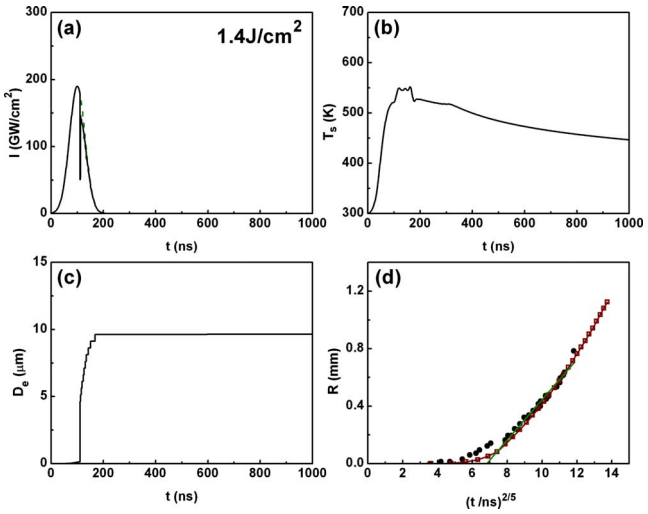

FIG. 2. (Color online) (a) Time profiles of laser irradiances with the total fluence of 1.4 J/cm^2. The original profile and the attenuated laser irradiance at the target surface are represented by dashed and solid lines, respectively. (b) Calculated surface temperature and (c) interface displacement for laser fluence 1.4 J/cm^2. (d) Comparison of experimental shock front position data (●) with our fluid dynamics calculations in the presence of phase explosion (□). Extrapolating the linear fit of the final $R(t)$ segment to $R=0$ provided onset time of phase explosion (solid line).

First, we show the simulation results for an intermediate laser fluence, 1.4 J/cm^2. Figure 2(a) presents the time profiles of the original laser pulse (dashed line) and the calculated laser irradiance at the liquid vapor interface. When the phase explosion occurs, a layer of water in the target becomes part of the plume, with an average density for the vapor-droplet mixture approaching that of the liquid water. Thus, the nonlinear absorption of laser light in this part of the plume becomes significant, i.e., during the phase explosion process the dense part of the plume (transformed directly from the water target) becomes opaque. As a result, some part of laser energy is directly absorbed by the plume after the onset of phase explosion. Laser energy deposition into the layer undergoing phase explosion had a nontrivial effect on the plume expansion dynamics because it coupled energy into this part of the plume. We found that when this absorption mechanism was excluded from the model, the plume expansion results showed poor agreement with the experimental data. Figure 2(a) indicates that the phase explosion at 1.4 J/cm^2 laser fluence begins at 110 ns. This value was adjusted from the 122 ns estimate we had obtained using the Taylor similarity fit (see Sec. II C) to achieve a better agreement with the experimental data.

When the phase explosion starts, the interface separating the vapor and superheated liquid recedes into the target with a dramatically increased rate. The calculated target surface temperature and interface displacement as a function of time are plotted in Figs. 2(b) and 2(c), respectively. Figure 2(c) indicates that the interface recedes by ~9.6 μm during the phase explosion process (from 110 ns to 167 ns). This dis-

placement cannot be viewed as an "ablation depth" as in the secondary processes at later times (>1 μs) significantly more liquid is ejected due to the recoil-induced pressure pulse. Moreover, in the case of a liquid target the ablation depth cannot be defined because the removed material is replenished from the surrounding volume. Nevertheless, we follow this quantity in the calculations to compare the effect of phase explosion to that of surface evaporation and gauge its efficiency in material removal during the early phase of the ablation at different laser fluence levels.

Approximately at 190 ns the phase explosion stopped because the flux of deposited laser energy was not sufficient to sustain it. From 110 ns to 190 ns, the calculated target surface temperature exhibited some oscillations between ~518 K ($0.8T_c$) and ~570 K. This artifact occurred because the simulations used a larger spatial step size for the plume domain than for the condensed phase. This allows us to follow the plume expansion for extended period (1 μs). Each time the phase explosion temperature is reached during the phase explosion process, several cells in the target domain are transformed into a single cell in the plume domain. Thus the calculated target surface temperature is slightly overestimated. However, this can be corrected by averaging the temperature in the transformed part before it is used in the plume domain calculation. The temperature profile in Fig. 2(b) shows the corrected temperature values. After the phase explosion stops, the calculated surface temperature slowly declines.

The comparison of the calculated shock front displacement with the experimental results is shown in Fig. 2(d). Both the measured values and the calculations show that the shock front displacement starts with an initial slower phase followed by a more vigorous accelerated expansion. Rescaling the data using the $t^{2/5}$ variable reveals two main slopes corresponding to the two expansion stages. The slow and the fast stages are thought to correspond to surface evaporation and phase explosion, respectively. The relative importance of the two energy dissipation mechanisms (surface and volume) can be inferred from Fig. 2(d). Based on the slope ratio of the two linear sections in Fig. 2(d), the ratio of energies used in the volume and surface processes is $E_v/E_s=105.5$. Thus of the 1.4 J/cm^2 total fluence, only ~0.013 J/cm^2, or ~1% is dissipated through the surface mechanism.

We can see that the simulation results follow the experimental data. The calculated shock front positions and slopes during the surface evaporation phase (short times) underestimate the experimental data by an approximate factor of 2. During the second period (phase explosion), however, the agreement is quite good. As most of the laser energy is utilized in the second ablation phase, this is an indication that the energy deposition and redistribution are accurately reflected in the model. The discrepancy at short times can be attributed to inhomogeneities in the laser beam cross section (hot spots) or to the inaccuracy of the description of surface evaporation (KL model).

B. Anatomy of the phase explosion

The temperature distributions in the target and plume domains before and during the phase explosion exhibit very

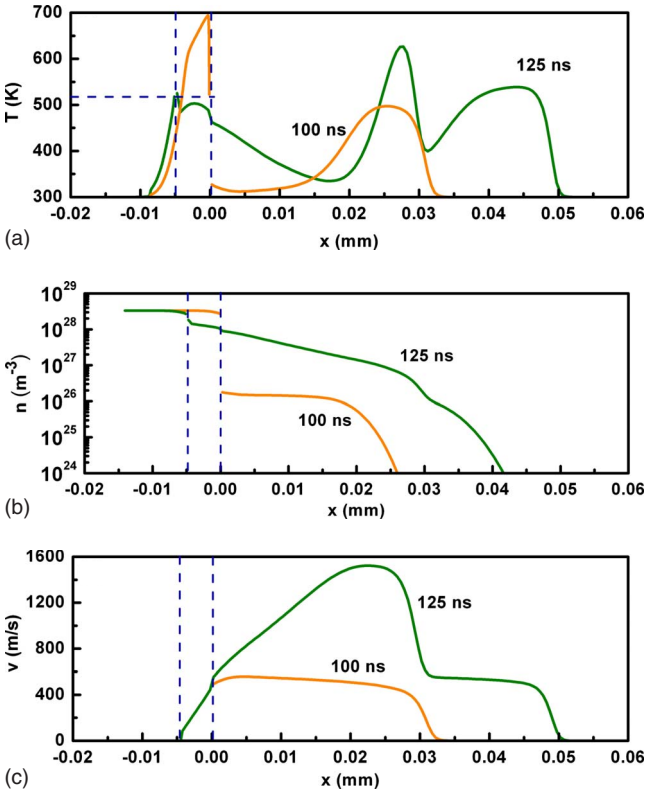

FIG. 3. (Color online) Spatial distribution of water (a) temperature, (b) number density, and (c) velocity in the target and plume domains for a fluence of 1.4 J/cm^2 at 100 ns (before phase explosion) and 125 ns (during phase explosion).

different features. As an example, Fig. 3(a) shows the spatial distributions before (at 100 ns) and during (at 125 ns) the phase explosion for a fluence of 1.4 J/cm^2. Vertical and horizontal dashed lines show the position of the interface at the two times and the phase explosion temperature ($0.8T_c$), respectively. The 100 ns profile indicates that the maximum temperature in the target before the phase explosion is found beneath the surface. This occurs because at the surface the vaporization removes some of the energy and because of the more efficient subsurface energy deposition due to the nonlinearity of the absorption. Temporarily the maximum temperature in the target may exceed both the phase explosion and for a shorter period the critical temperature because of sudden superheating. Also, before the phase explosion there is a large temperature gradient at the interface between the target and the plume due to the presence of the KL. In the plume domain, there is a high temperature region close to the shock front due to the heating effect of the shockwave.

During the phase explosion, the interface separating the target and the plume domains is shifted in the direction of the target by, for example, 5 μm at 125 ns. Unlike before the phase explosion, at this stage the maximum temperature appears at the interface. As a result of the high vapor density created by the phase explosion adjacent to the target surface, direct absorption of the laser light by the plume is observed there that minimizes the temperature difference across the interface. This direct absorption of energy by the plume produces the additional structure in the plume temperature pro-

file during phase explosion. For other times during the 57 ns long phase explosion the features of the 125 ns profile evolve due to the plume expansion, thus we do not show the results here.

The logarithmic water number density distributions in the target and plume domains are presented in Fig. 3(b). Before the phase explosion (100 ns) at the interface the number density decreases discontinuously due to the relatively slow surface vaporization. This creates a dense vapor plume that is still ~150 lower than the density of the liquid. Once phase explosion starts, a layer of liquid water is suddenly converted into a mixture of vapor and fine droplets. The number density of water in this mixture layer is comparable to that of the target. Thus the number density of water across the interface becomes quasicontinuous and the large gradient observed in the 100 ns profile disappears.

The velocity distributions at 100 and 125 ns are shown in Fig. 3(c). Before phase explosion, e.g., at 100 ns, there is only a single shockwave in the plume, whereas during the phase explosion, e.g., at 125 ns, a second shockwave appears. This is due to the additional energy deposition and water transfer directly into the plume. Moreover, there is a large difference in the plume velocity value at the target surface. Due to the strong surface vaporization process, at 100 ns it is ~500 m/s, whereas at 125 ns, the velocity value at the retracted interface is close to zero. This is due to the drastically reduced momentum flux across the interface separating the liquid water and the vapor. It should be pointed out that the velocity distributions are only calculated in the plume domain. During the phase explosion process, the velocity at the interface separating the liquid water and the vapor is evaluated based on the temperature and mass density gradients across the interface.

C. Background gas effects

In order to explore the effect of the background gas on the plume dynamics, we compared the expansion in 1 atm environment and in vacuum. The time progression of the density distributions is shown in Fig. 4(a) for the first 800 ns of plume expansion following a 1.4 J/cm^2 laser pulse at atmospheric pressure. The formation of a shock front at the contact between the expanding plume and the background gas manifests in steep density gradients. The figure also shows an elevated plume density near the shock front and a significantly increased background gas pressure ahead of it known as the pile-up or "snowplow" effect.

At the early stage of plume expansion, the separation between the vapor and the ambient gas is well defined, i.e., the contact layer is very thin, ~20 μm at 200 ns. Due to the binary diffusion process (partly also due to accumulated numerical error), at later stages, the contact layer becomes thicker and the vapor and the ambient gas are mixed together. For example at 800 ns the thickness of this mixed layer is ~66 μm. Due to the nature of the model (single velocity for the plume) this value does not include convective mixing. In agreement with experimental observations, the pile-up effect in the background gas results in a significant slowdown in plume expansion for atmospheric pressure

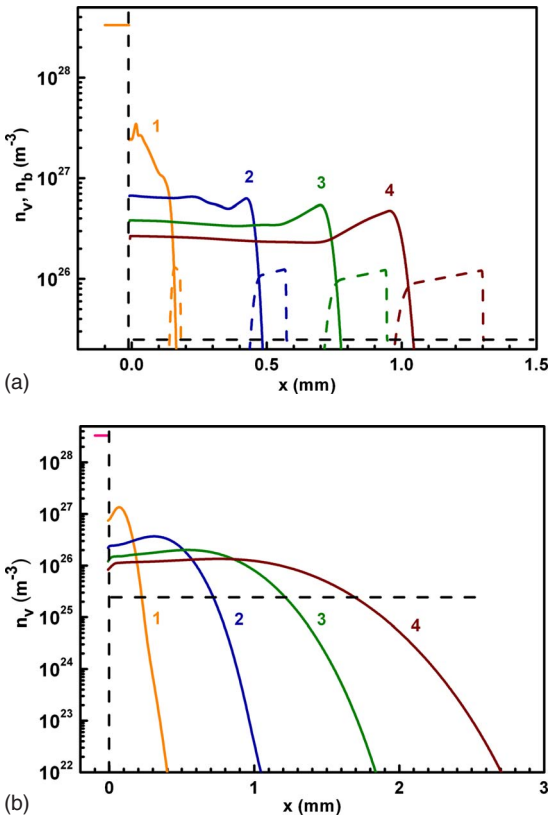

FIG. 4. (Color online) Time progression of plume number density distributions for 1.4 J/cm^2 Er:YAG laser ablation of water into (a) 1 atm nitrogen gas and (b) vacuum at 200 ns (1), 400 ns (2), 600 ns (3), and 800 ns (4). The distributions in (a) show a high density region close to the shock front and the pileup of background gas in front of the interface. Solid lines indicate water vapor density, whereas the dashed lines denote background gas density. Horizontal dashed lines indicate the gas density at atmospheric pressure.

laser ablation. This can be seen by comparing Fig. 4(a) with Fig. 4(b) that presents the plume expansion into vacuum under the same conditions. At 800 ns, the ablated material reaches the density of the atmospheric pressure environment at 1.0 mm in the presence of the ambient gas, but it exhibits the same density at 1.7 mm in the vacuum case. As a consequence, the material ablated in ambient gas remains denser for a longer time than in vacuum. In the case of nucleating and/or reacting laser plumes this results in enhanced cluster formation and/or higher concentration of reaction products.

D. Elevated and low fluence regimes

To assess the range of validity for the model, we also performed the simulations for elevated and low laser fluences, 5.4 and 0.12 J/cm^2, respectively. Figure 5(a) shows the time profiles of the incoming 5.4 J/cm^2 laser pulse and the calculated fluence at the plume-target interface. For this elevated fluence the phase explosion starts already when the laser pulse reaches its peak irradiance at ~100 ns and lasts for 87 ns. In order to achieve a better agreement with the experimental data, the start time value was adjusted from the 87 ns estimate we had obtained using the Taylor similarity fit

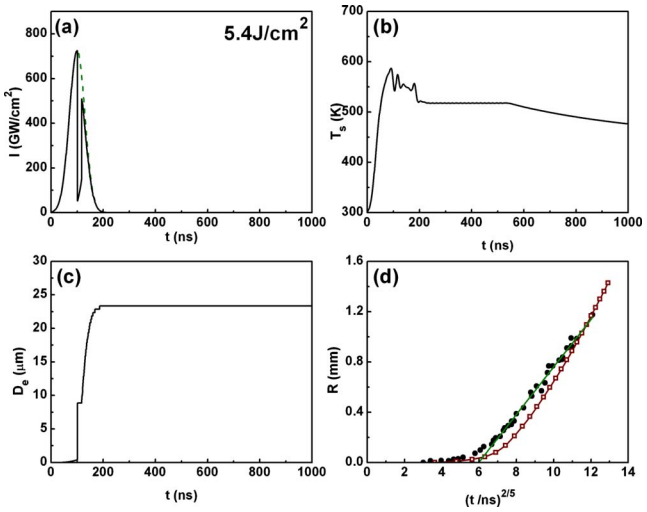

FIG. 5. (Color online) (a) Temporal laser irradiance profiles for a total fluence of 5.4 J/cm^2. The incident laser irradiance and the attenuated laser irradiance at the surface are represented by solid and dashed lines, respectively. (b) Calculated surface temperature and (c) interface displacement for laser fluence 5.4 J/cm^2. (d) Comparison of experimental shock front position data (●) for 5.4 J/cm^2 laser fluence with our fluid dynamics calculations (□). Extrapolating the linear fit of the final $R(t)$ segment to $R=0$ provided onset time of phase explosion (solid line).

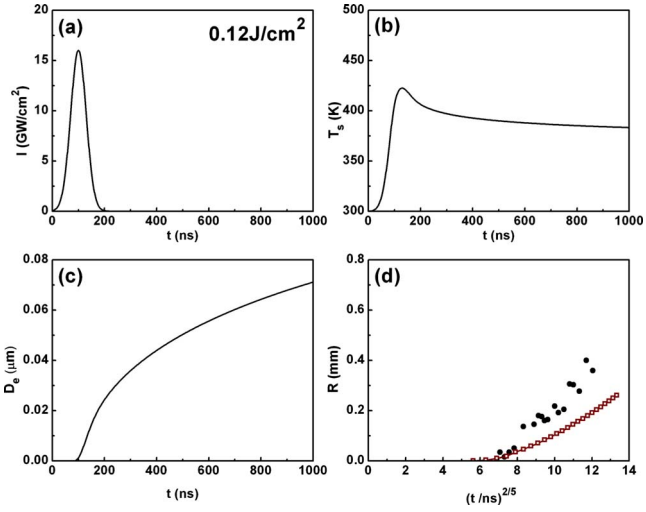

FIG. 6. (Color online) (a) Temporal laser irradiance profiles for a total fluence of 0.12 J/cm^2. The incident laser irradiance is indistinguishable from the irradiance arriving to the interface (optically thin plume). Compared to the two higher fluences in Figs. 2 and 5, (b) significantly lower surface temperatures and (c) interface displacements are calculated for 0.12 J/cm^2 laser fluence. (d) Comparison of experimental shock front position data (●) for 0.12 J/cm^2 laser fluence with our fluid dynamics calculations (□).

(see Sec. II C) to 100 ns. Comparing Fig. 5(a) with Fig. 2(a) reveals that for the 5.4 J/cm^2 case the phase explosion starts earlier, produces a more opaque plume, and lasts longer than for the 1.4 J/cm^2 case.

Figure 5(b) shows that after the phase explosion the calculated surface temperature, T_s, is sustained almost constant at 518 K and only starts to decrease at 550 ns. This is because the pressure of the vapor in the plume domain adjacent to the interface is larger than or similar to the saturation pressure calculated at $0.8T_c$ and thus there is neither further phase explosion nor vaporization. This is reflected in Fig. 5(c) showing that, after a dramatic increase during the phase explosion process between 100 and 187 ns, there is no additional interface displacement.

Figures 2(c) and 5(c) indicate interface displacements for the 1.4 and 5.4 J/cm^2 laser fluences as 9.6 and 23.4 μm, respectively. Due to the increasingly opaque plumes at higher laser fluences the ablation depth grows slower than linear, i.e., the 5.4 J/cm^2 laser pulse leads to a denser vapor than the pulse at 1.4 J/cm^2 fluence, which in turn reduces the laser irradiance that reaches the target.

Comparison of calculated shock front displacement and the experimental data for 5.4 J/cm^2 laser fluence, presented in Fig. 5(d), demonstrate good agreement at early times. As time progresses, but still in the surface evaporation regime, the calculations increasingly underestimate the shock front position, eventually by as much as 50%. Once the phase explosion starts the calculated values start to approach the experimental observations closer and closer and by the end of the observation period there is good agreement.

The slope ratio for the two linear sections of the experimental plot is $s=2.57$, which corresponds to a ratio of energies expended in the volume and surface processes, $E_v/E_s=111$, assuming that the thermal energy absorbed by the target is negligible. Thus, the overwhelming majority of the deposited energy is utilized in the phase explosion process. In particular, of the 5.4 J/cm^2 laser fluence only 0.05 J/cm^2 drives the surface evaporation, whereas the remaining 5.35 J/cm^2 is used for the volume process.

At substantially reduced laser fluences the nature of expansion dynamics changes. Figure 6 shows the simulation results for such a laser fluence (0.12 J/cm^2). It is clear from Fig. 6(b) that in this case there is no phase explosion. Indeed, the temporal surface temperature profile does not reach $0.8T_c$ throughout the 1 μs period. Although in principle some subsurface layers could still reach the phase explosion temperature, the lack of plume absorption in Fig. 6(a) and the very low rate of interface displacement indicate that phase explosion does not occur. Comparing Figs. 6(a) and 6(b) one can also notice that when the laser irradiance reaches its peak value at 100 ns, the calculated surface temperature does not exhibit its maximum value yet. The time delay between the two maxima is ~30 ns. During this period the deposited laser energy still exceeds the sum of energy dissipated by heat conduction, consumed by the latent heat of the phase transition and lost due to the surface evaporation.

Material loss through the interface is gauged by the displacement of the interface as a function of time [see Fig. 6(c)]. It is interesting to compare the total displacements, 0.07, 9.6, and 23.4 μm, for the three studied fluences of 0.12, 1.4, and 5.4 J/cm^2, respectively. Although the laser fluence between its low and intermediate value only increases by a factor of 12, the corresponding interface displacement rises by a factor of 140. This disproportionate response is due to the onset of phase explosion that dramatically accel-

erates material removal. The corresponding fluence ratio between the intermediate and elevated fluence case are 3.9, whereas the displacement ratio is 2.4. As both the intermediate and elevated fluence case exhibit phase explosion, there is no disproportionate change in this case. On the contrary, the increasing optical thickness of the plume reduces the laser heating of the condensed phase.

Thus the interface displacement is a highly nonlinear function of laser fluence due to three factors: the onset of phase explosion at a certain fluence value, the self-screening of the target by the plume absorption and the inherent nonlinearity of mid-IR light absorption by liquid water.

Comparison of the calculated shock front position data to the experiments for the case of 0.12 J/cm^2 in Fig. 6(d) reveals large discrepancies. Except for the initial four data points (<170 ns), the calculated shock front positions as well as their slope as a function of $t^{2/5}$ are lower than the measured data by approximately a factor of 2. The sources of this difference are hard to identify. It seems like there is a weak phase explosion occurring in the experiment, but the temperatures calculated with the assumptions made for the fluence do not approach the value necessary for this effect. This can be explained by considering the cross sectional intensity distributions in the laser beam. Assuming that the delivered laser pulse exhibited Gaussian (TEM_{00}) distribution, the average intensity we used in the 1D calculation did not represent the central higher intensity area properly. This means that the center of the Gaussian distribution could have initiated phase explosion in that region. Similarly, if the beam profile contained so called hot spots they could have also led to local superheating of the sample. To obtain experimental data for a better comparison with the 1D simulation, a top-hat beam profile produced by mode scrambling in an optical fiber would be more suitable. Alternatively, radial intensity variations in the laser beam could be incorporated into a two-dimensional calculation.

IV. CONCLUSIONS

We introduced a 1D fluid dynamics model for water-rich target ablation by midinfrared laser pulses that predicted the shock front displacement during plume expansion in the presence of both surface evaporation and phase explosion. We showed that both the nonlinear absorption coefficient of water and the effect of phase explosion in the target were essential to obtain reasonable agreement with the experiments in the intermediate (1.4 J/cm^2) to elevated (5.4 J/cm^2) fluence range. At low (0.12 J/cm^2) fluences the incorporation of laser intensity distribution across its cross section is probably necessary to explain the data.

The simulation results confirmed that due to two different phase transition mechanisms the first, slower plume expansion phase was followed by a more vigorous accelerated expansion phase. It was demonstrated that the phase explosion was much more efficient in ablating material than surface vaporization. Above the onset of phase explosion, the interface displacement as a function of laser fluence grew slower than linear due to the optical screening of the target by the produced plume. It should be pointed out that the onset time of phase explosion cannot be derived from the fluid dynamics model. From the perspective of the kinetic theory, phase explosion is a process of homogeneous bubble nucleation in a superheated, metastable liquid. When the bubble radius exceeds a critical radius, phase explosion starts. Thus it is possible to estimate the time needed for the growing bubbles to reach the critical radius (see Ref. [29]). However, because the surface tension of water greatly varies with temperature and the fluctuation of liquid density becomes very large close to the critical temperature, the estimated value for the onset time of phase explosion exhibits a very large uncertainty. Due to these large uncertainties in the presented model we did not use the values estimated by the kinetic theory. Instead we derived estimated values from the experimental data using the Taylor similarity model. These values were slightly ($<15\%$) modified to achieve better agreement between the fluid dynamics results and the experiments. Accurate prediction of the phase explosion onset time requires the description of nucleation and growth kinetics for the vapor regions, a difficult problem that is beyond the scope of this paper.

The current 1D fluid dynamics model cannot predict the rich variety of processes (vortex formation, mushroom cloud, plume collapse, splashing, etc.) in water ablation and the plume expansion dynamics at later stages (e.g., at times beyond 1 μs). There are two primary reasons for this limitation. First, at these later stages of the ablation, the three-dimensional nature of the plume expansion becomes more noticeable. Second, due to the recoil-induced pressure, the dynamic instabilities at the interface and the associated liquid ejection, the radial transport of material becomes very significant. These processes require at least two-dimensional treatment (assuming cylindrical symmetry) in the axial and radial directions.

The presented analysis focused on water ablation. In most applications of mid-IR laser ablation the target is a biological tissue. This is true both for chemical analysis and in medical applications. In these cases the model also needs to include the behavior of the target under stress. Material parameters, including compressive, tensile, and shear strength become very important in determining the onset of substantial material ejection. Modeling the role of these processes also requires at least two-dimensional description.

Although the effects discussed above are not included in the presented model, the 1D approach is useful to assess the contribution of phase explosion to the plume expansion dynamics at the early stage in water-rich target ablation and it can be used in better understanding analytical (AP-MALDI), preparative (MAPLE), and medical (surgery) applications.

ACKNOWLEDGMENTS

We are grateful for the insightful comments and for the sharing of, at the time unpublished, data by A. Vogel. This research was supported by the U.S. Department of Energy (Contract No. DE-FG02-01ER15129), by the W. M. Keck Foundation (Contract No. 041904), and by the Research Enhancement Fund of the George Washington University.

[1] M. von Allmen and A. Blatter, *Laser-Beam Interactions with Materials*, 2nd ed. (Springer, Berlin, 1995), pp. 1–94.
[2] A. Peterlongo, A. Miotello, and R. Kelly, Phys. Rev. E **50**, 4716 (1994).
[3] R. F. Wood, K. R. Chen, J. N. Leboeuf, A. A. Puretzky, and D. B. Geohegan, Phys. Rev. Lett. **79**, 1571 (1997).
[4] S. S. Harilal, C. V. Bindhu, V. P. N. Nampoori, and C. P. G. Vallabhan, Appl. Phys. Lett. **72**, 167 (1998).
[5] N. M. Bulgakova, A. V. Bulgakov, and O. F. Bobrenok, Phys. Rev. E **62**, 5624 (2000).
[6] J. H. Yoo, S. H. Jeong, X. L. Mao, R. Greif, and R. E. Russo, Appl. Phys. Lett. **76**, 783 (2000).
[7] N. M. Bulgakova, I. M. Bourakov, and N. A. Bulgakova, Phys. Rev. E **63**, 046311 (2001).
[8] H. Kim, J. S. Horwitz, G. P. Kushto, Z. H. Kafafi, and D. B. Chrisey, Appl. Phys. Lett. **79**, 284 (2001).
[9] Q. M. Lu, S. S. Mao, X. L. Mao, and R. E. Russo, Appl. Phys. Lett. **80**, 3072 (2002).
[10] D. Perez and L. J. Lewis, Phys. Rev. Lett. **89**, 255504 (2002).
[11] P. Lorazo, L. J. Lewis, and M. Meunier, Phys. Rev. Lett. **91**, 225502 (2003).
[12] T. E. Itina, J. Hermann, P. Delaporte, and M. Sentis, Phys. Rev. E **66**, 066406 (2002).
[13] A. Bogaerts, Z. Y. Chen, R. Gijbels, and A. Vertes, Spectrochim. Acta, Part B **58**, 1867 (2003).
[14] B. J. Garrison, T. E. Itina, and L. V. Zhigilei, Phys. Rev. E **68**, 041501 (2003).
[15] A. Pique, R. A. McGill, D. B. Chrisey, D. Leonhardt, T. E. Mslna, B. J. Spargo, J. H. Callahan, R. W. Vachet, R. Chung, and M. A. Bucaro, Thin Solid Films **356**, 536 (1999).
[16] J. Li and G. K. Ananthasuresh, J. Micromech. Microeng. **11**, 38 (2001).
[17] Q. Y. Fang and X. H. Hu, IEEE J. Quantum Electron. **40**, 69 (2004).
[18] D. B. Geohegan, A. A. Puretzky, G. Duscher, and S. J. Pennycook, Appl. Phys. Lett. **72**, 2987 (1998).
[19] V. V. Laiko, N. I. Taranenko, V. D. Berkout, M. A. Yakshin, C. R. Prasad, H. S. Lee, and V. M. Doroshenko, J. Am. Soc. Mass Spectrom. **13**, 354 (2002).
[20] R. E. Russo, X. L. Mao, and S. S. Mao, Anal. Chem. **74**, 70A (2002).
[21] D. M. Bubb, J. S. Horwitz, J. H. Callahan, R. A. McGill, E. J. Houser, D. B. Chrisey, M. R. Papantonakis, R. F. Haglund, Jr., M. C. Galicia, and A. Vertes, J. Vac. Sci. Technol. A **19**, 2698 (2001).
[22] I. Apitz and A. Vogel, Appl. Phys. A: Mater. Sci. Process. **81**, 329 (2005).
[23] Y. Li, B. Shrestha, and A. Vertes, Anal. Chem. **79**, 523 (2007).
[24] V. V. Laiko, M. A. Baldwin, and A. L. Burlingame, Anal. Chem. **72**, 652 (2000).
[25] P. Nemes and A. Vertes, Anal. Chem. **79**, 8098 (2007).
[26] Y. Li, B. Shrestha, and A. Vertes, Anal. Chem. **80**, 407 (2008).
[27] H. C. Le, D. E. Zeitoun, J. D. Parisse, M. Sentis, and W. Marine, Phys. Rev. E **62**, 4152 (2000).
[28] R. Kelly and A. Miotello, Phys. Rev. E **60**, 2616 (1999).
[29] J. H. Yoo, S. H. Jeong, R. Greif, and R. E. Russo, J. Appl. Phys. **88**, 1638 (2000).
[30] Q. M. Lu, Phys. Rev. E **67**, 016410 (2003).
[31] R. K. Shori, A. A. Walston, O. M. Stafsudd, D. Fried, and J. T. Walsh, IEEE J. Sel. Top. Quantum Electron. **7**, 959 (2001).
[32] Z. Y. Chen and A. Bogaerts, J. Appl. Phys. **97**, 063305 (2005).
[33] Z. Chen, A. Bogaerts, and A. Vertes, Appl. Phys. Lett. **89**, 041503 (2006).
[34] http://www.engineeringtoolbox.com/water-thermal-properties-d_162.html (last accessed 13 September 2007).
[35] R. Kelly and A. Miotello, Nucl. Instrum. Methods Phys. Res. B **91**, 682 (1994).
[36] G. Taylor, Proc. R. Soc. London, Ser. A **201**, 159 (1950).